

Unified formulations for RKKY interaction, side Kondo behavior, and Fano antiresonance in a hybrid tripartite quantum dot device with filtered density of states

Jia-Ning Wang,^{1,2} Wang-Huai Zhou,^{1,2} Yu-Xiong Yan,¹ Wei Li,^{1,2} Nan Nan,^{1,2} Jun Zhang,^{1,2} Ya-Nan Ma,¹
Peng-Chao Wang,^{1,2} Xiang-Rui Ma,^{1,2} Shi-Jun Luo¹ and Yong-Chen Xiong^{1,2,*}

¹*School of Mathematics, Physics and Optoelectronic Engineering, and Collaborative Innovation Center for Optoelectronic Technology, Hubei University of Automotive Technology, Shiyan 442002, People's Republic of China*

²*Shiyan Industrial Technology Research Institute of Chinese Academy of Engineering, Shiyan 442002, People's Republic of China*



(Received 7 March 2022; revised 17 July 2022; accepted 18 July 2022; published 27 July 2022)

Hybrid quantum dot structures are potential building blocks for spintronic devices and quantum logic gates, within which the understanding of many-body correlations is a prerequisite for implementing quantum information processing and generating controlled entanglement. Herein, we consider a hybrid tripartite quantum dot device, one of which is embedded directly between the source and drain electrodes, while the other two dots are side coupled to the first one. Modeling the system using the three-impurity Anderson model, we concentrate on the Ruderman-Kittel-Kasuya-Yosida interaction, the suppression of the Kondo behavior in the side dots, the destructive quantum interference, the gate-controlled quantum phase transitions, the Dicke effect, the ferromagnetic Kondo effect, and the thermodynamical properties in various parameter regimes using the numerical renormalization group method. Unified formulations are established, which are associated with the effective width of the zero-energy peak of the central dot without side dots, the central-side exchange coupling, as well the on-site electron-electron repulsion. We demonstrate that these formulas are well suitable for the non-, weak-, and strong-interacting cases.

DOI: [10.1103/PhysRevB.106.035428](https://doi.org/10.1103/PhysRevB.106.035428)

I. INTRODUCTION

Since the early 2000s, low-dimensional quantum impurity systems have gained tremendous interests, due to their unexpected anomalies and ubiquitous applicability to plentiful physical systems, such as magnetic impurities [1,2], dissipative two-level systems [3,4], semiconductor quantum dots (QDs) [5–7], molecular break junction [8,9], clusters of magnetic adsorbates on surfaces of noble metals [10,11], heavy-fermion compounds and other strongly correlated systems [12–14]. Numerically, these systems are always described by *ab initio* studies. However, for strongly correlated systems, the *ab initio* description of transport measurements remains to date a challenge [15]. One of the most important strongly correlated phenomena arising in these systems is the Kondo effect, which is caused by the interaction between a localized spin and conduction electrons via the spin-flip scattering process [12,16,17]. Even since J. Kondo did the third-order perturbation theory and observed that it was divergent at low energies [18], and K. G. Wilson explained this interesting behavior perfectly based on the renormalization group theory [19], the Kondo effect has then invoked some of the most profound concepts in condensed matter physics. Recently, profiting from the advances in experimental micro- and nanotechnologies, resurgent interests have been seen in discovering novel Kondo physics in low-dimensional quantum impurity structures, such as the orbital Kondo effect [20,21],

the underscreened Kondo effect [22–24], the overscreened Kondo effect [25,26], the ferromagnetic Kondo effect [24,27], the multistage Kondo effect [28–30], the topological Kondo effect [31,32], as well the Kondo effect in unconventional host materials. For instance, the Kondo effect on the surface of three-dimensional topological insulators [33,34], the pseudogap Kondo effect [35,36], the power-law Kondo model [37,38], and the Kondo effect in Dirac and Weyl systems [39,40].

Distinguishing from those phenomena observed in single-impurity models, additional elements may emerge in multiple-impurity models, among which the most fascinating one is the RKKY exchange interaction [41]. Basically, the RKKY interaction generates when a few impurities interconnected by the conduction baths, which then leads to magnetic coupling of moments between different impurities. It plays an important role in quantum impurity systems. For instance, it may lead to long range magnetic orders and result in various magnetic ground states [42]. It may also bring about different transport properties of multi-impurity systems [13,43–45] and Aharonov-Bohm interferometers [46,47]. Additionally, competitions between the RKKY interaction and different local interactions may lead to various kinds of quantum phase transitions (QPTs) [48–50] and quantum interferences [51,52]. It is also proved to be essential for the development of quantum computing and quantum precision measurement [53,54] and the spintronic and tunneling magnetoresistance devices [55,56].

Generally speaking, there exist two mechanisms of the interimpurity RKKY interaction: the

*xiongyc_lx@huat.edu.cn

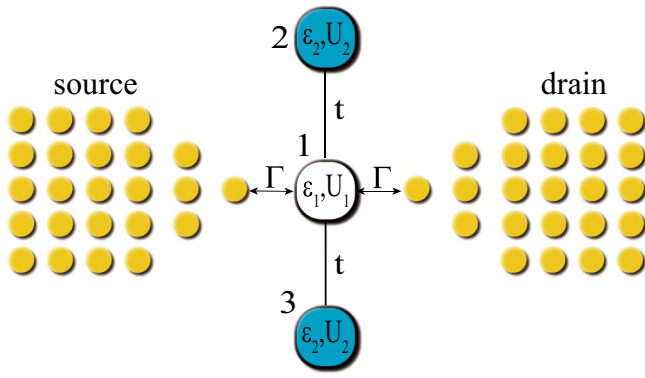


FIG. 1. Schematic illustration of the hybrid tripartite QD device connected to the source (S) and drain (D) electrodes. The device contains three functional quantum dots (QDs), each of which has a single transport-active orbital. The QD 1 is the central QD (CQD), while the QDs 2 and 3 are the side QDs (SQDs). ϵ_i and U_i are the energy levels and the on-site electron-electron repulsion of the i th QD, respectively. Γ is the hybridization function between the CQD and the conduction bands, and t is the interdot hopping integral (tunneling coupling).

noninteracting-conduction-band mediated RKKY interaction, and the superexchange one mediated via the interimpurity electron hopping. The former one is found to be associated with the band-impurity hybridization Γ and the on-site Coulomb interaction U in the local impurities with a relation $\propto \Gamma^2/U$, which is valid in the broadband limit with a constant density of states (DOS) [57]. And the latter one could be understood from perturbative arguments [58]. However, little is known about the case where the RKKY-interaction-ordered impurities connect to a structured nonconstant DOS. A universal scheme for such cases is highly desired.

To implement such an idea, we considered a triple impurity Anderson model with one impurity (the central impurity) sandwiched between the source (S) and drain (D) electrodes, whereas the other impurities (side impurities) only connect to the central one through interimpurity hopping t , see Fig. 1. We mainly focus on the case where the central impurity is effectively noninteracting, whereas the side impurities are fully interacting. Under such a situation, the present model maps onto a double impurity Anderson model with a structured nonconstant DOS. Our main findings include the following. When the central-side hopping integral t is absent, the linear conductance reaches its unitary limit, which stems from the resonant tunneling due to a level broadening imposed on the central impurity by the conduction baths. When t is present, the interference between the direct and indirect conduction pathways brings about a Fano antiresonance dip in the local DOS (LDOS) of the central impurity. We reveal the width of this dip W_F could be illustrated by an exponential function of the electrode-central hybridization function Γ and the central-side exchange interaction J . For small nonzero t , three kinds of energy peaks could be clarified in the LDOS of the side impurities, including the Coulomb, the RKKY, and the Kondo peaks. The intensity of the RKKY interaction J_{RKKY} could be well illustrated by a function of Γ , t , and the electron-electron repulsion on the side impurities U_2 . For large t , only one kind

of spectral peak survives, corresponding to the energy needed to add an additional electron to the system. The Kondo effect could be found in the side impurities, which is suppressed gradually as t increases. The height of the Kondo peak h_K is found to be associated with Γ and t via an exponential function but has no connection to U_2 . Thermodynamic properties show that the local spins are screened in two steps occurring at about Γ and T_K^* respectively, separated by a scale of J_{RKKY} . We show the Kondo temperature T_K^* could also be described by an exponential function of Γ and J , distinguishing from the typical two-stage Kondo effect. The above conclusions are found to be also suitable for the weakly- and strongly correlated central impurities by replacing Γ appropriately. Furthermore, by tuning the charge of the central impurity, the spin correlation between two side impurities transits from an antiferromagnetic type to a ferromagnetic one, and then to an antiferromagnetic one, regardless of whether the central impurity is strongly or noncorrelated. We attribute the enhancement of the conductance to the Dicke effect, which is resulted from the quantum interference between the direct and the indirect couplings. When the Coulomb repulsion in the central impurity is adjusted, our present structure acts as an ideal prototype revealing a crossover from an effective parallel two-impurity model to the ferromagnetic Kondo state, and h_K is found to be associated with the effective width of the zero-energy peak of the central impurity without side ones.

One notices that real triple impurity structures could be those clusters of magnetic adsorbates on various kinds of substrates, such as Co and Fe adsorbates on the CuN/Cu(100) surface [59], Co atoms adsorbed on Cu/Co/Cu(100) multilayers [60], manganese phthalocyanine (MnPc) molecule on Au(111) surface [61]. They could also be repeating conjugated monomer units connected to metal electrodes [62,63] and systems of triple semiconductor quantum dots [64,65]. However, these structures are predominantly limited to homogeneous species, and thus it is difficult to meet the expectation of unidentical Coulomb repulsion in different impurities. Ideal candidates to verify our theoretical predictions may be those hybrid QD devices containing triple transport-active orbitals or triple spin-1/2 subsystems. For instance, a supramolecular spintronic device based on a carbon nanotube quantum dot functionalized with modified molecular magnets [66,67], a tripartite system consisting of two molecular spin qubits rings and a nonmagnetic ion [68], systems of organic diradical bridged by magnetic/nonmagnetic ion [69,70], and the rare-earth molecular trinuclear coordination compounds [71]. In such cases, the central impurity plays a role as the electronic QD, whereas the side impurities could be considered as the spin QDs [67].

The remaining part of this paper is organized as follows: In Sec. II, we give the Hamiltonian of the considered system and present the calculate method and basic formulas. In Sec. III–Sec. VI, we show the numerical results and their discussions. Finally, a conclusion is given.

II. MODEL, METHOD, AND FORMULAS

Schematic illustration of the hybrid tripartite QD device is given in Fig. 1. The related second quantized Hamiltonian

could be written as follows [8,17]:

$$H = H_v + H_{\text{HTQD}} + H_{\text{hyb}}; \quad (1)$$

$$H_v = \sum_{v=S,D} \sum_{k\sigma} \epsilon_{vk\sigma} c_{vk\sigma}^\dagger c_{vk\sigma}; \quad (2)$$

$$H_{\text{HTQD}} = \sum_{i\sigma} \epsilon_i d_{i\sigma}^\dagger d_{i\sigma} + \sum_{i\sigma} U_i n_{i\uparrow} n_{i\downarrow} - t \sum_{\sigma} (d_{1\sigma}^\dagger d_{2\sigma} + d_{1\sigma}^\dagger d_{3\sigma} + \text{H.c.}); \quad (3)$$

$$H_{\text{hyb}} = \tau \sum_{vk\sigma} (c_{vk\sigma}^\dagger d_{1\sigma} + \text{H.c.}). \quad (4)$$

Here H_v illustrates the noninteracting S and D electrodes. $c_{vk\sigma}^\dagger$ is the creation operator for electrons with wave vector k , spin σ ($=\uparrow$ or \downarrow) in lead v , and $\epsilon_{vk\sigma}$ is the energy level with respect to the Fermi level. H_{HTQD} is for electrons on the hybrid tripartite QD device. $d_{i\sigma}$ ($d_{i\sigma}^\dagger$) annihilates (creates) a local electron from (on) the i th QD ($i = 1, 3$), and $n_{i\sigma} = d_{i\sigma}^\dagger d_{i\sigma}$ is the spin- σ number operator. ϵ_i and U_i are the single electron energy and the on-site Coulomb repulsion, respectively. Experimentally, ϵ_i could be tuned via external gate voltage. Hereafter, QD 1 is denoted as the central QD (CQD), while QDs 2 and 3 are the side QDs (SQDs). t is the hopping integral (tunneling coupling) between the CQD and SQDs. Finally, H_{hyb} describes the band-CQD coupling, with τ be the tunneling strength. Here we assume τ is k and σ independent and is symmetric with respect to the S and D electrodes.

We adopt the Wilson's numerical renormalization group (NRG) method [17,72,73] to handle Eq. (1). The NRG method is a nonperturbative technique to treat quantum impurity models, which gives sufficient information on both the static and dynamic properties in the whole temperature scales. In our NRG calculation, we choose the renormalization parameter Λ to be ~ 2.0 – 3.0 and retain around 3000 low-lying states at each iteration. In the NRG technique, Λ divides the conduction band into a series of intervals, whose widths decrease exponentially. Furthermore, we denote the half bandwidth of the conduction band as W_b and take a wide flat DOS of the electrodes $\rho = 1/(2W_b)$, which is the typical case relevant to most metallic electrodes. The hybridization function between the conduction band and the CQD then could be written as $\Gamma = \pi \rho \tau^2$.

The LDOS of each QD at temperature T $A_i(\omega, T)$ is defined as

$$A_i(\omega, T) = \sum_{\sigma} A_{i\sigma}(\omega, T) = -\frac{1}{\pi} \sum_{\sigma} \text{Im} G_{ii\sigma}(\omega, T). \quad (5)$$

Here ω is the energy variable, $G_{ii\sigma}(\omega)$ is the Fourier transformation of the diagonal retarded Green's function $G_{ii\sigma}(t)$, with

$$G_{ij\sigma}(t) = -i\theta(t) \langle \{d_{i\sigma}(t), d_{j\sigma}^\dagger\} \rangle. \quad (6)$$

In the following, we abbreviate $A_i(\omega, T)$ at zero temperature as $A_i(\omega)$.

The linear conductance through the device $G(T)$ is computed by the Landauer formula [74,75]:

$$G(T) = G_0 \int \left[-\frac{\partial f(\omega)}{\partial \omega} \right] \pi \Gamma A_1(\omega, T) d\omega. \quad (7)$$

Here $G_0 = 2e^2/h$ is the conductance quantum, $f(\omega) = 1/[1 + \exp(\omega/T)]$ is the Fermi-Dirac distribution function. In the following discussions, we chose W_b as the energy unit and $\epsilon_{k_F} = 0$ as the Fermi level. Hence $G(T = 0)$ at zero temperature in the limit of zero bias is controlled by the behavior of $A_1(\omega, T)$ at the Fermi level,

$$G(T = 0) = \pi \Gamma G_0 A_1(\omega = 0). \quad (8)$$

To enhance the precision, those dynamical quantities, such as spectral functions, are obtained from the full density matrix (FDM) [76], calculated iteratively in the Anders-Schiller basis [77].

The temperature-dependent magnetic moment $\mu^2(T)$ and entropy $S_{\text{HTQD}}(T)$ are given by the contribution of the device to the total magnetic moment and entropy of the whole system, respectively:

$$\begin{aligned} \mu^2(T) &= \chi_{\text{HTQD}}(T) k_B T / (g \mu_B^2) \\ &= \langle \mathbf{S}_z^2 \rangle - \langle \mathbf{S}_z \rangle_0, \end{aligned} \quad (9)$$

$$S_{\text{HTQD}}(T) = \frac{(E - F)}{T} - \frac{(E - F)_0}{T}, \quad (10)$$

where χ_{HTQD} is the contribution of the QDs to the total magnetic susceptibility at temperature T . k_B is the Boltzmann's constant, g is the electric gyromagnetic factor, and μ_B is the Bohr magneton. \mathbf{S}_z is the total z component spin operator of the QDs, and the subscript 0 refers to the situation when the QDs are absent. Finally, $E = \langle H \rangle = \text{Tr}[H e^{-H/(k_B T)}]$ and $F = -k_B T \ln \text{Tr}[e^{-H/(k_B T)}]$ are the total energy and free energy of the whole system, respectively.

III. NONINTERACTING CQD WITH $U_1 = 0$ AND $U_2 \neq 0$

A. The destructive quantum interference characteristic antiresonance

In the following discussions, we mainly focus on the situation where ϵ_i satisfies the particle-hole (p-h) symmetry, i.e., $\epsilon_i = -U_i/2$. In Fig. 2(a), we depict the LDOS of electrons in QD 1 at nearly zero temperature $A_1(\omega)$ in terms of different t with fixed $U_1 = \epsilon_1 = 0$. One may see when $t = 0$, there is a peak of the Lorentzian type located at the Fermi level. For later references, we denote $A_1(\omega)$ without t as $A_1^0(\omega)$. The characteristic energy scale is that the width of this peak W_L is about 2Γ , suggesting that the electron transport is dominated by the resonant tunneling due to a level broadening imposed on the CQD by both external reservoirs of the itinerant electrons. Here W_L is defined by the full width at half maximum of the central peak. In such a case, the linear conductance is given by a Breit-Wigner-type expression [78]

$$G(\epsilon_{k_F}) = G_0 \frac{\Gamma^2}{(\epsilon_1 - \epsilon_{k_F})^2 + \Gamma^2}. \quad (11)$$

Thus at exact resonance, $\epsilon_1 = \epsilon_{k_F} = 0$, the conductance reaches its maximal value G_0 . On the other hand, with the aid of the Green's function, $A_1^0(\omega)$ can be expressed as

$$A_1^0(\omega) = \frac{\Gamma}{\pi [(\omega - \epsilon_1)^2 + \Gamma^2]}, \quad (12)$$

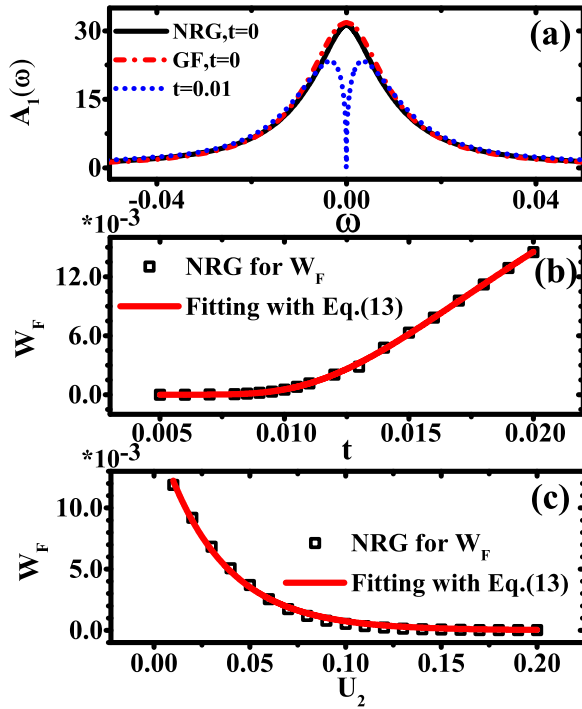


FIG. 2. (a) The LDOS of electrons in QD 1 at nearly zero temperature $A_1(\omega)$ with and without t . Here $A_1(\omega)$ without t , labeled by $A_1^0(\omega)$ hereafter, is calculated by both the NRG method (solid black line) and the Green's function (GF, dashed-dotted red line). [(b) and (c)] The width of the Fano antiresonance dip W_F at nearly zero temperature as functions of t (b) and U_2 (c) and their fitting functions. The other parameters are given by $\Gamma = 0.01$, $U_1 = 0.0$, $U_2 = 0.1$, $t = 0.01$, and $\epsilon_i = -U_i/2$ unless otherwise specified.

which is also shown in Fig. 2(a). It is seen the results calculated by the NRG method matches very well with that by the Green's function. This is a good test for our NRG results.

When t turns on, e.g., $t = 0.01$ in Fig. 2(a), the Lorentzian peak splits, and a dip at $\omega = 0$ develops, which is the so-called Fano antiresonance dip. This behavior could be attributed to a destructive interference of the quantum amplitudes for the conduction pathway directly through the CQD without passing through the SQDs and the indirect conduction pathway via the SQDs. The first pathway could be considered as a role of the broad background process, while the second one refers to a resonant scattering channel. With increasing t (U_2), the width of the Fano dip W_F increases (decreases), see the scattered squares in Figs. 2(b) and 2(c). Here W_F is defined by the full width at half maximum of the central valley. More importantly, it is found that W_F could be illustrated by an exponential function of t , U_2 , and Γ :

$$W_F = c_1 \Gamma e^{-c_2 \Gamma / J}, \quad (13)$$

with $c_1 = 4.38$, $c_2 = 3.52$ in Fig. 2(b), and $c_1 = 1.66$, $c_2 = 2.48$ in Fig. 2(c). This expression is similar to that for the second Kondo temperature in the two-stage Kondo behavior, which always exists in side-coupled multi-QDs structures [79–82]. Here J is the effective exchange coupling between

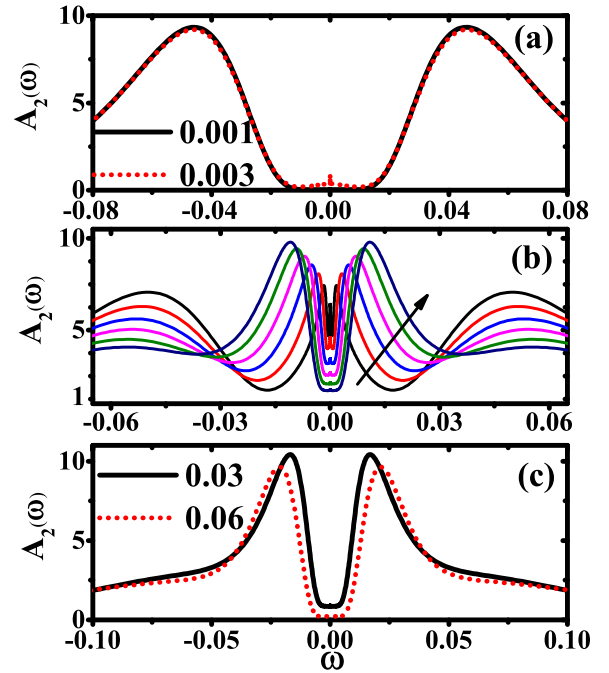


FIG. 3. [(a)–(c)] The LDOS of electrons in QD 2 (3) at nearly zero temperature $A_2(\omega)$ for different t . Curves in panel (b) along the black solid line are for $t = 0.011$ to 0.021 in steps of 0.002 , respectively. The other parameters are given the same as in Fig. 2 unless otherwise specified.

the central and side QDs and could be written as

$$J = \frac{2t^2}{\epsilon_1 - \epsilon_2 + U_1} + \frac{2t^2}{\epsilon_2 - \epsilon_1 + U_2}. \quad (14)$$

Obviously, with $U_1 = \epsilon_1 = 0$, $J = 8t^2/U_2$. One notices that the fitting functions are consistent with our NRG results.

B. The RKKY interaction

The most fascinating behaviors occur in the SQDs. In Fig. 3, we plot the LDOS of electrons in QD 2 (3) at nearly zero temperature $A_2(\omega)$ for various t . The species of the energy peaks seem to undergo three different regimes. When t is small, only the Coulomb peaks are found at about $\omega = \pm U_2/2$. For intermediate t , three kinds of peaks could be clarified clearly. Except the Coulomb peaks, one observes a sharp peak at the Fermi level, which is the Kondo resonant peak as will be discussed detailedly in the following subsection. The additional pair between the Kondo and Coulomb peaks are the RKKY peaks. They correspond to the RKKY interaction between electrons in different side QDs mediated by t and stem from the processes of creating (annihilating) an additional electron to (from) the many-body states of the side QDs with antiparallel spin, where two electrons on the side QDs have parallel spins. As t increases, the locations of the RKKY J_{RKKY} peaks move backward with respect to each other [cf. Fig. 3(b)]. When t is large enough, such that $J \gg \Gamma$, only one pair peak exists [cf. Fig. 3(c)]. Since in this case the SQDs are in the molecular-orbital (MO) regime. The effect of the Coulomb repulsion becomes feeble, which is reflected by the decreasing weight of the Coulomb peaks. The new

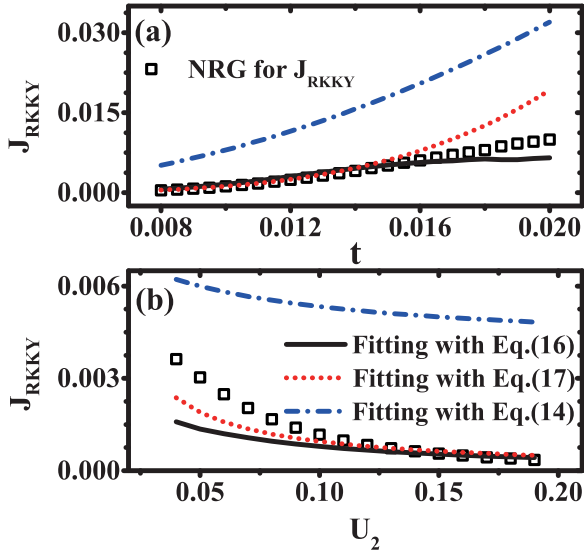


FIG. 4. [(a) and (b)] The magnitude of the RKKY interaction between side QDs J_{RKKY} versus t (a) and U_2 (b), and their fitting functions simulated through Eqs. (16), (17), and (14), respectively. The other parameters are given the same as in Fig. 2 unless otherwise specified.

peaks refer to the energy needed to add (remove) an additional electron to (from) the SQDs, which is proportional to t [83]. With decreasing U_2 , $A_2(\omega)$ behaves in a similar way as that of increasing t , which is not shown here.

To make a deep understanding of the RKKY interaction, we present J_{RKKY} captured by our NRG calculations and its fitting functions in Fig. 4. In parallel multiple quantum dot systems connected to noninteracting conduction bands with constant DOS, the Rayleigh-Schrödinger perturbation theory gives $J_{\text{RKKY}} \propto U(\rho J_K)^2$ [57]. Here U is the on-site Coulomb repulsion in the parallelly organized quantum dots, J_K is the effective antiferromagnetic Kondo exchange interaction between the conduction bands and the quantum dots, and $\rho J_K = 8\Gamma/(\pi U)$. In our present model, all information on the couplings of the side dots to the leads and to the central dot could be illustrated by the effective hybridization function between the central and side QDs:

$$\Gamma_{c-s}(\omega) = \pi A_1^0(\omega)t^2, \quad (15)$$

and the RKKY interaction is mediated by t . Therefore, it is feasible to simulate the RKKY interaction by the following formula:

$$J_{\text{RKKY}} = c_3 U_2 \left[A_1^0(\omega_{\text{RKKY}}) \frac{8t^2}{U_2} \right]^2, \quad (16)$$

with $c_3 = 0.25$ in Fig. 4(a) and 0.125 in Fig. 4(b). Here ω_{RKKY} is the energy (frequency) corresponding to J_{RKKY} . One notices they are consistent with our NRG results in the regime $U_2 \gg t$, see the solid black curves in Figs. 4(a) and 4(b). However, Fig. 4 also indicates that if t/U_2 is large enough, then the location of the peak deviates from the above relationship, due to the SQDs are in the MO regime. One observes that there is no sharp boundary between the RKKY and MO regimes; instead, these two regimes are smoothly connected.

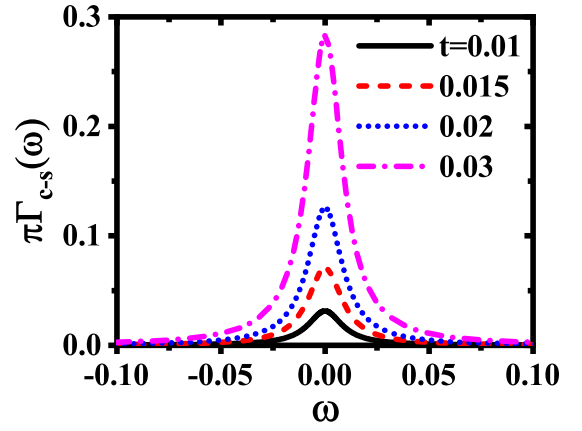


FIG. 5. Effective hybridization function between the central and side QDs $\pi \Gamma_{c-s}(\omega)$ in terms of different t . The remaining parameters are the same as Fig. 2.

The deviation also could be attributed to the following picture. When t grows, $\Gamma_{c-s}(\omega)$ increases. If t is large enough, e.g., $t = 0.02$, then $\pi \Gamma_{c-s}(\omega)$ around $\omega = 0$ exceeds U_2 , see Fig. 5. Thus above relation becomes invalid, because the perturbation theory requires $U_2 \gg \pi \Gamma_{c-s}(\omega)$.

On the other hand, if $U_2/t \gg 1$, then the RKKY peaks are very close to the Fermi level. One then acquires a more efficient way to estimate J_{RKKY} . Fixing $\epsilon_1 = 0$, and taking the value of $A_1^0(\omega)$ at the Fermi surface, $A_1^0(0) = 1/(\pi\Gamma)$ [cf. Eq. (12)]. One then obtains

$$J_{\text{RKKY}} = c_4 \frac{t^4}{U_2 \Gamma^2}. \quad (17)$$

It is found this equation agrees very well with the numerical results in the RKKY regime with $c_4 = 1.2$ in Fig. 4(a) and 0.8 in Fig. 4(b). Therefore, this formula is very helpful for evaluating the scale of J_{RKKY} . Furthermore, we stress that when t is particularly small, i.e., t in Fig. 3(a), the RKKY peaks as well the Kondo peak do exist in $A_2(\omega)$ theoretically; however, the orders are too small to be captured by numerical techniques.

In addition, since Eq. (1) does not contain the item of the RKKY interaction, and creating (annihilating) an additional electron to (from) the many-body states of the SQDs also relates to the exchange interaction J , one may think that the additional peaks are produced by J , viz. Eq. (14). To clarify this viewpoint, we also depict J versus t and U_2 in Figs. 4(a) and 4(b), respectively. It is seen the line shape of J deviates significantly from those of our NRG results, indicating the additional peaks are definitely not produced by J .

C. The suppression of the side Kondo behavior

From Fig. 2(a), one knows that the peak located at $\omega = 0$ in $A_1(\omega)$ disappears once t turns on. However, as mentioned in Sec. III B, the zero-energy peak in turn raises in $A_2(\omega)$, corresponding to the Kondo resonance in the side dots. Henceforth, we denote it as the *side Kondo behavior*, differing from the regular Kondo effect which always occurs in those quantum impurities sandwiched between different conduction baths [12,17]. In this case, our present model maps onto a parallelly

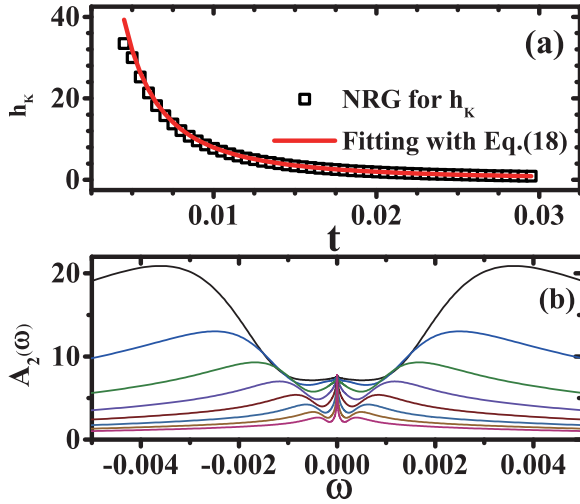


FIG. 6. (a) The height of the Kondo peak h_K at nearly zero temperature versus t and its fitting function. (b) Enlarged scale of $A_2(\omega)$ for various U_2 . The curves from the top to the bottom are for $U_2 = 0.04$ to 0.18 in steps of 0.02 , respectively. The remaining parameters are the same as Fig. 2.

organized double QDs coupled to a Fermi system with an effective hybridization function $\Gamma_{c-s}(\omega)$, which “filters” the band states seen by the side QDs and modifies their couplings to the leads [84]. As a result, the side Kondo effect generates due to the exchange coupling J .

Furthermore, one finds that the side Kondo effect may only persist for small t . As t increases, the height of the Kondo peak h_K decreases continuously. When t grows to the MO regime, the Kondo effect is totally suppressed [cf. Figs. 3(b)–3(c)]. In Fig. 6(a), we show h_K as a function of t . One finds the evolution of h_K could be matched by a function of t and Γ :

$$h_K = c_5 \frac{\Gamma}{\pi t^2}, \quad (18)$$

with $c_5 = 0.25$. In the standard single impurity Anderson model with constant Γ , the height of the Kondo peak could be illustrated by $h_K = 1/(\pi\Gamma)$ [12]. In our present model, the hybridization function $\Gamma_{c-s}(\omega)$ becomes nonconstant, and thus we replace Γ with $\Gamma_{c-s}(0)$, giving a perfect fitting function of h_K , viz., Eq. (18). Meanwhile, one also finds that h_K is smaller by a factor of c_5 than the standard result for a flat band with the same hybridization strength.

Equation (18) also indicates that h_K has no connection with U_2 . To verify this picture, we show $A_2(\omega)$ in terms of different U_2 in an enlarged scale in Fig. 6(b). It is clear that h_K , i.e., the ordinate of $A_2(\omega = 0)$, does not change as U_2 sweeps. However, if U_2 is small, e.g., $U_2 = 0.04$, then the spectral weight turns to be flat in the vicinity of $\omega = 0$, and hence the Kondo effect is also suppressed. In fact, Eq. (18) could be obtained through the Friedel sum rule, which bridges the local spectral weight with the charge occupation in the QDs [85,86]. Since in our present studies each QD is at half-filling ($\epsilon_i = -U_i/2$) with the charge number holding at 1.0 by symmetry, thus h_K does not depend on U_2 .

To make a deep understanding of this side Kondo behavior, we show $A_1(\omega)$ and $A_2(\omega)$ at nearly zero temperature for $t =$

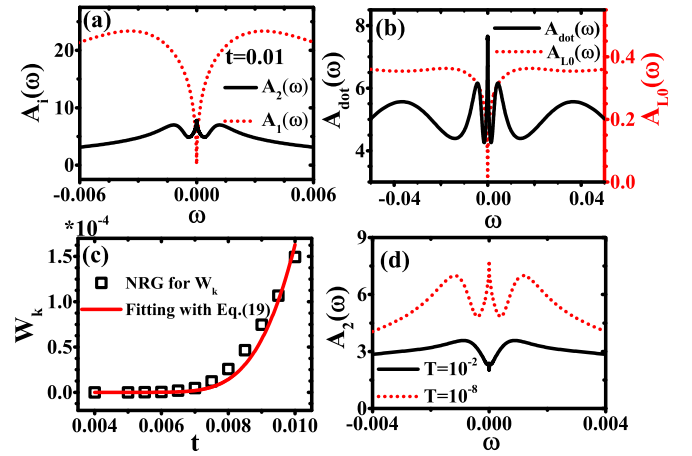


FIG. 7. (a) LDOS $A_i(\omega)$ of the CQD and SQDs at nearly zero temperature for $t = 0.01$. (b) LDOS of each dot $A_{\text{dot}}(\omega)$ and DOS of the first site in the conduction lead $A_{L0}(\omega)$ at nearly zero temperature for a PDQD system with identical Coulomb repulsion 0.1 and dot-lead hybridization 0.01. (c) The width of the side Kondo peak W_K in $A_2(\omega)$ and its fitting expression as functions of t . (d) $A_2(\omega)$ for temperatures $T > J$ (e.g., $T = 10^{-2}$) and $T < J$ (e.g., $T = 10^{-8}$) with $t = 0.01$, respectively. The remaining parameters are the same as Fig. 2 unless otherwise specified.

0.01 in Fig. 7(a). One notices that the line shape of $A_2(\omega)$ and $A_1(\omega)$ near $\omega = 0$ are quite similar to the DOS of the quantum dots $A_{\text{dot}}(\omega)$ and the first site of the conduction lead $A_{L0}(\omega)$ in the general parallel double quantum dot (PDQD) system, respectively, which are given in Fig. 7(b). These phenomena indicate that the peak located at the Fermi level of $A_2(\omega)$ is assuredly resulted from the Kondo behavior. In fact, in our present model, the CQD could be considered as a new bath, with spectral function $A_1^0(\omega)$. Since this effective bath is still metallic with $U_1 = 0$, one may expect essentially identical behaviors in the SQDs, similar to the case of general PDQD structure.

In Fig. 7(c), we show the t dependence of the width of the side Kondo peak W_K . We notice that W_K could be fitted by an exponential function of J and $A_1^0(\omega = 0) = 1/(\pi\Gamma)$:

$$W_K = c_6 U_2 \sqrt{A_1^0(\omega = 0)} J e^{-1/[A_1^0(\omega = 0)J]}, \quad (19)$$

with $c_6 = 0.164$. This relation is similar to the Haldane’s expression [87]. For a reference, please see Eq. (21). Interestingly, c_6 is very close to that in the modified Haldane’s expression in Ref. [57]. Additionally, we also plot $A_2(\omega)$ for different temperature scales T in Fig. 7(d), typically for $T > J$ (e.g., $T = 10^{-2}$) and $T < J$ (e.g., $T = 10^{-8}$), respectively. One finds the peak at $A_2(\omega = 0)$ reveals a typical Kondo-type temperature variation, where for $T > J$, there is no Kondo peak at the Fermi surface, whereas it emerges if $T < J$ [88]. These behaviors confirm again that the narrow peak at $A_2(\omega = 0)$ is definitely resulted from the Kondo effect.

D. The thermodynamics properties

The above results are for zero temperature, more interesting phenomena could be found at finite temperatures. In

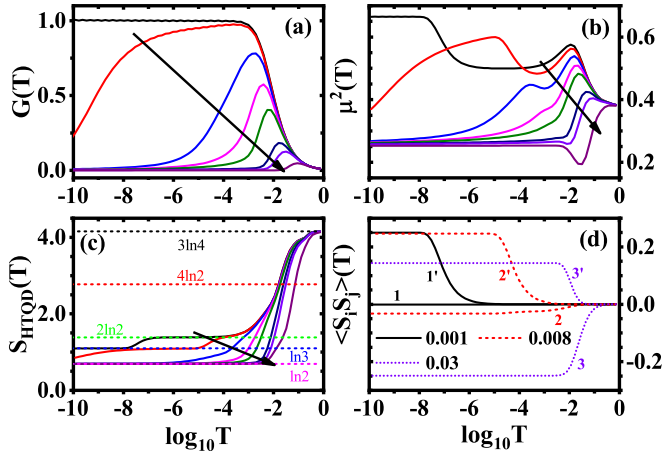


FIG. 8. Temperature-dependent (a) $G(T)$, (b) local magnetic moment $\mu^2(T)$, (c) entropy $S_{\text{HTQD}}(T)$, and (d) spin-spin correlation $\langle S_i S_j \rangle(T)$ between QDs i and j for the QD device. Curves in panels (a)–(c) along the black arrow are for $t = 0.001$ – 0.017 in steps of 0.004 , 0.03 , 0.04 , and 0.1 , respectively. Curves in panel (d) are for $t = 0.001$, 0.008 , and 0.03 respectively. Those labeled by 1–3 in this panel are results for $\langle S_1 S_2 \rangle$, whereas 1'–3' are for $\langle S_2 S_3 \rangle$. The remaining parameters are the same as in Fig. 2.

Fig. 8, we show the linear conductance $G(T)$, the local magnetic moment $\mu^2(T)$, the entropy $S_{\text{HTQD}}(T)$, and the spin-spin correlation $\langle S_i S_j \rangle(T)$ between QDs i and j for the device versus $\log_{10} T$. The uppermost curve in Fig. 8(a) is for small $t \ll \Gamma$, e.g., $t = 0.001$. At high temperature with $T \gg \Gamma$ and $T > U_2$, $G(T) \approx 0$ for all t . Because in this temperature scale, local electrons in the device are independent, and the many-body states $|0\rangle$, $|\uparrow\rangle$, $|\downarrow\rangle$, and $|2\rangle$ in each QD are equally probable. Each QD then contributes $1/8$ to $\mu^2(T)$ and $\ln 4$ to $S_{\text{HTQD}}(T)$, resulting in total quantities $\mu^2(T) = 3/8$ and $S_{\text{HTQD}}(T) = 3\ln 4$, accompanied by $\langle S_i S_j \rangle \approx 0$, see Figs. 8(b)–8(d).

When T decreases to the regime $\Gamma < T \leq U_2$, U_2 , which favors singly occupied states in the SQDs, starts to play an important role. States $|0\rangle$ and $|2\rangle$ in the SQDs are then suppressed, and each SQD contributes $1/4$ to $\mu^2(T)$ and $\ln 2$ to $S_{\text{HTQD}}(T)$. Hence $\mu^2(T) = 1/2 + 1/8 = 5/8$ and $S_{\text{HTQD}}(T) \approx 2\ln 2 + \ln 4 = 4\ln 2$. Here our numerical results for $\mu^2(T)$ only reach about 0.6 , and the platform of $4\ln 2$ in $S_{\text{HTQD}}(T)$ is not obvious, for a finite U_2 is employed. By tuning U_2 upwards, one may expect that $\mu^2(T)$ in this regime grows gradually, accompanied by a notable platform of $4\ln 2$ in $S_{\text{HTQD}}(T)$ if U_2 is large enough.

As T decreases to the scale of Γ , the hybridization develops between electrons on the CQD and those on the conduction baths, due to Γ . Hence $G(T)$ increases gradually to its unitary limit G_0 due to the level broadening of the local orbital in the CQD. In this case, the electron spin on the CQD is screened and has no contribution to $\mu^2(T)$ and $S_{\text{HTQD}}(T)$, resulting in $\mu^2(T) \approx 1/2$ and $S_{\text{HTQD}}(T) \approx 2\ln 2$.

Below Γ , the resonant tunneling holds, and one may find a large plain in $\mu^2(T)$ and $S_{\text{HTQD}}(T)$. However, when T decreases to the scale of J_{RKKY} , $\mu^2(T)$ increases continuously to about 0.7 . Because in this temperature scale, the RKKY interaction between two SQDs turns to be pronounced. The local

spins on the SQDs are then arranged ferromagnetically, which is confirmed by $\langle S_2 S_3 \rangle$ growing to about 0.25 in Fig. 8(d). The device then locks into a high spin state with a total residual spin $S_{\text{tot}} = 1$, bringing $\mu^2(T) = S_{\text{tot}}(S_{\text{tot}} + 1)/3 = 2/3$ and $S_{\text{HTQD}}(T) = \ln(2S_{\text{tot}} + 1) = \ln 3$.

For larger t , the resonant tunneling is suppressed gradually at low temperature, and hence $G(T)$ deviates from its maximum value [cf. $t = 0.005$ in Fig. 8(a)]. Furthermore, one also notices that the temperature T_K^* where $G(T)$ weakens to zero increases with growing t , suggesting that the temperature window where the resonant tunneling taking place becomes more and more narrow, see along the black arrow in Fig. 8(a). Under such a situation, a Kondo singlet generates between electrons in the CQD and those in the SQDs, which suppresses the antiferromagnetic coupling between electrons in the CQD and those in the conduction bands, and the Lorentzian peak splits and decreases gradually [cf. $t = 0.01$ in Fig. 2(a)]. Meanwhile, spins on the SQDs are partially screened by that on the CQD through t at a certain temperature T_K^* , leading to a residual spin $S_{\text{tot}} = 1/2$. As a result, $\mu^2(T) = 1/4$ and $S_{\text{HTQD}}(T) = \ln 2$ in the regime $T < T_K^*$.

When t is in the MO regime, e.g., $t = 0.03$, 0.04 , and 0.1 , the coupling between the central and side QDs becomes extremely strong [cf. Fig. 8(d)]. Spin singlet between the central and side QDs develops at a higher temperature than that between the CQD and the conduction bands due to $t > \Gamma$. Therefore, the $G(T) = G_0$ state is totally suppressed in nearly all temperature scales, $\mu^2(T) = 1/4$ and $S_{\text{HTQD}}(T) = \ln 2$ then hold in a large regime of T . Furthermore, the local spin now reveals an interesting window of diamagnetic behavior with $\mu^2(T) < 1/4$, which becomes more and more significant as t increases, and is accompanied by the suppression of the side Kondo behavior in $A_2(\omega)$. This phenomenon is similar to those findings of a negative magnetic susceptibility in narrow-band systems [89]. For decreasing U_2 , the evolutions of $G(T)$, $\mu^2(T)$, $S_{\text{HTQD}}(T)$, and $\langle S_i S_j \rangle(T)$ are similar to the above behaviors, hence we neglect them here.

To make a deep understanding of T_K^* against t and U_2 , we depict T_K^* and its fitting functions versus t and U_2 in Figs. 9(a) and 9(b), respectively. Here T_K^* is defined by the temperature corresponding to the half maximum of $\mu^2(T)$ where the device decreases from the high spin state to $1/4$ at low temperature. One finds T_K^* could be described by a function of Γ and J :

$$T_K^* = c_7 \Gamma e^{-c_8 \Gamma/J}, \quad (20)$$

with the fitting parameters are given by $c_7 = 0.12$, $c_8 = 2.58$ in Fig. 9(a) and $c_7 = 0.07$, $c_8 = 2.17$ in Fig. 9(b), respectively. It is seen that the fitting functions are consistent with our NRG results. This behavior is similar to the two-stage Kondo effect in the side-coupled double quantum dot system [79,80]. However, singular phenomena could be identified. In the typical two-stage Kondo effect, local spins are screened by two processes at different Kondo temperatures T_K and T_K^* , accompanied by the appearance and the disappearance of the Kondo resonant peak in the central impurity, respectively, whereas in our present model, the first screening process does not refer to the Kondo effect, and hence Eq. (20) does not contain the element of T_K . Here T_K is the regular Kondo temperature without t . Second, in the typical two-stage Kondo effect, both

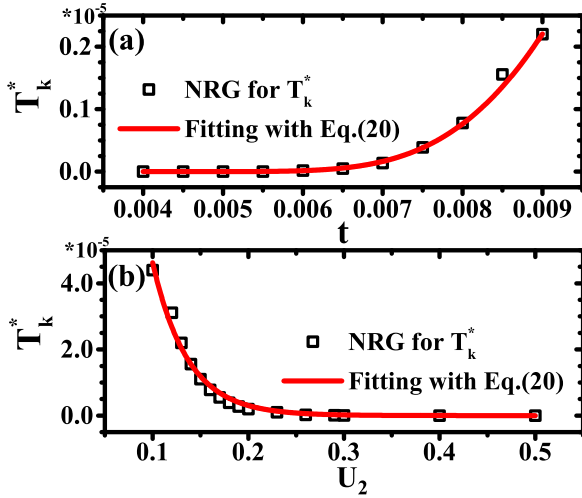


FIG. 9. T_K^* as functions of (a) t and (b) U_2 , respectively. Scatter plots are captured from our NRG data, while the solid curves are the fitting functions. The other parameters are the same as in Fig. 2.

the fitting parameters c_7 and c_8 are some constants of order 1, which are also distinguished from ours. Because in our present model, the two screening processes are separated by a RKKY temperature scale J_{RKKY} . Thus T_K^* becomes extremely low comparing with the first screening temperature 2Γ , and c_7 is much lower than that in the side-coupled double quantum dot system [79,80]. Additionally, it is worth to be noted that there should be theoretically a second drop occurring in $G(T)$, $\mu^2(T)$, and $S_{\text{HTQD}}(T)$ at T_K^* for $t_1 = 0.001$ [cf. Figs. 8(a)–8(c)]. However, in such a case, Eq. (20) gives a $T_K^* \sim 10^{-143}$, and hence it is extremely difficult to be captured in both related experiments and theoretical simulations.

As a summary of this section, when $U_1 = 0$, the CQD could be considered as a new bath, with spectral function $A_1^0(\omega)$, and hence our present model maps to a PDQD model with a Lorentzian-type DOS, whose width is nearly 2Γ . We have established formulas for the Fano antiresonance, the RKKY interaction, and the side Kondo behaviors. More importantly, it is found that for this kind of structured nonconstant DOS, the Kondo physics seems only associate with the DOS at the Fermi level.

IV. FULLY INTERACTING CQD WITH $U_1 = 0.1$ AND $U_2 \neq 0$

A. The Fano antiresonance

The above results are restricted for the noninteracting case of the CQD, it is quite interesting to check its applicability for the strong-interacting case. In Fig. 10(a), we depict $A_1(\omega)$ for various t with $U_1 = U_2 = 0.1$. When t is zero, a Kondo peak emerges at $\omega = 0$, with a characteristic width equals to T_K . Here T_K is the Kondo temperature of the single impurity Anderson model, which could be estimated through the Haldane's expression [87]:

$$T_K = U_1 \sqrt{\rho J_C} e^{-1/(\rho J_C)}, \quad (21)$$

with $\rho J_C = 8\Gamma/(\pi U_1)$ is the effective coupling between the conduction bands and the CQD. When t becomes nonzero,

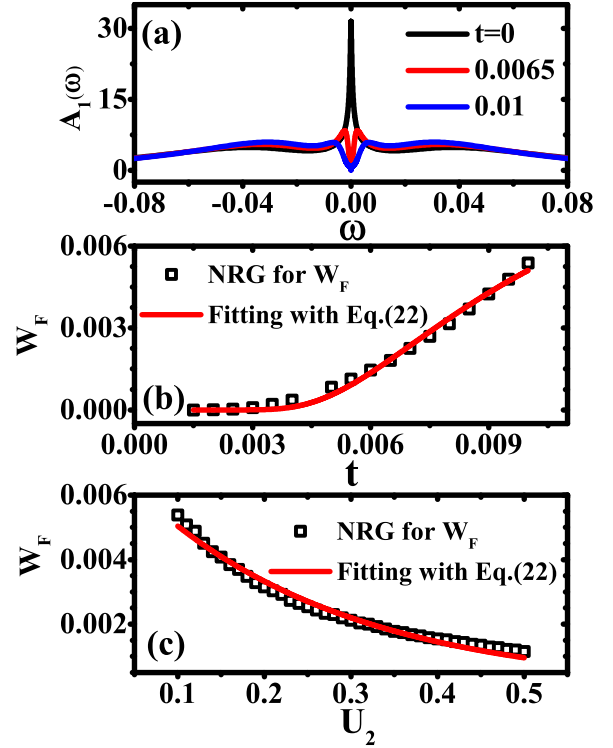


FIG. 10. (a) $A_1(\omega)$ at nearly zero temperature with and without t . [(b) and (c)] The width of the Fano antiresonance dip W_F at nearly zero temperature as functions of t (b) and U_2 (c) and their fitting functions. The other parameters are given by $\Gamma = 0.01$, $U_1 = U_2 = 0.1$, $t = 0.01$, and $\epsilon_i = -U_i/2$ unless otherwise specified.

the Fano antiresonance also appears, and hence the Kondo peak splits gradually as t increases. In Figs. 10(b) and 10(c), we describe the width of the Fano dip W_F and its fitting expressions as functions of t and U_2 , respectively. We find that W_F could be described by an exponential function of t and T_K :

$$W_F = c_9 T_K e^{-c_{10} T_K / J}, \quad (22)$$

with $c_9 = 1.08$ and $c_{10} = 0.30$ in Fig. 10(b) and $c_9 = 11.62$ and $c_{10} = 3.34$ in Fig. 10(c). We remind that J is given by Eq. (14).

B. The RKKY interaction

In Figs. 11(a) and 11(c), we depict $A_2(\omega)$ at nearly zero temperature in terms of different t and U_2 , respectively. One may see the side Kondo behavior hardly develops in the SQDs. However, the evolution of J_{RKKY} is similar to the case of $U_1 = 0$ [cf. Fig. 3, Fig. 11(a), and Fig. 11(c)]. J_{RKKY} versus $t^4/(U_2 T_K^2)$ and its fitting function are presented in Fig. 11(b) (sweeping t) and Fig. 11(d) (sweeping U_2), respectively. Scattered squares are captured in $A_2(\omega)$ of our NRG results. Equation (16) now turns to be

$$J_{\text{RKKY}} = c_{11} U_2 [A_1^0(\omega_{\text{RKKY}}) J]^2. \quad (23)$$

with J is given by Eq. (14). On the other hand, for finite U_1 , the ground state of the CQD is expected to be a Fermi liquid having an effective bandwidth T_K and a LDOS at the Fermi surface $A_1^0(0) \sim 1/(\pi T_K)$ [79,81]. We then replace Eq. (17)

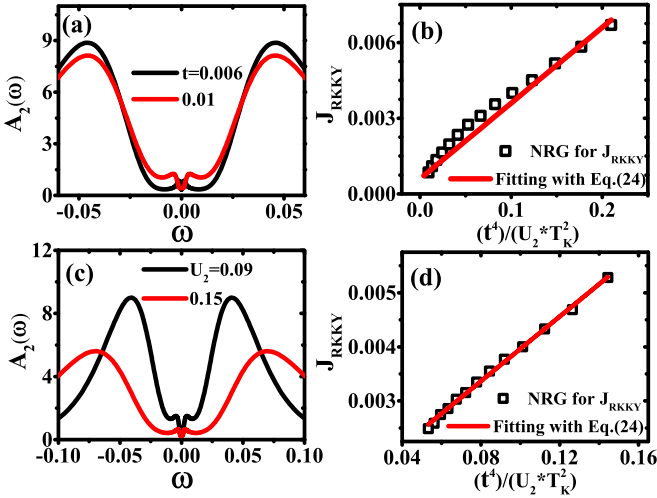


FIG. 11. $A_2(\omega)$ at nearly zero temperature in terms of different (a) t and (c) U_2 . J_{RKKY} and its fitting functions versus $t^4/(U_2 T_K^2)$ by sweeping (b) t and (d) U_2 , respectively. The remaining parameters are the same as Fig. 10 unless otherwise specified.

with the following equation:

$$J_{\text{RKKY}} = c_{12} \frac{t^4}{U_2 T_K^2}. \quad (24)$$

In Figs. 11(b) and 11(d), we show the results fitted by Eq. (24). One may see in both panels that Eq. (24) has a good agreement with the numerical results with $c_{12} = 0.03$ in both panels. However, on the other hand, Eq. (23) only matches with our NRG results in a small regime of t or U_2 , which are not shown here [for a reference, please see Fig. 14(b) for $U_1 = 0.01$]. For strong repulsion U_1 , the fitting functions by Eq. (23) deviate from the NRG results very quickly with increasing t or U_2 . Therefore, J_{RKKY} at its root only associates with the LDOS of $A_1^0(\omega)$ at the Fermi surface.

C. The thermodynamics properties

Figures 12(a)–12(c) show the temperature-dependent $G(T)$, $\mu^2(T)$, and $S_{\text{HTQD}}(T)$, respectively. When $\Gamma < T < U_i$ and t is small, e.g., $t = 0.0005$, each dot is singly occupied, with the many-body states $|\uparrow\rangle$ and $|\downarrow\rangle$ equally probable. Thus $\mu^2(T) \approx 3/4$ and $S_{\text{HTQD}}(T) \approx 3\ln 2$. For $T < T_K \approx 1.01 \times 10^{-3}$, the local spin on the CQD is screened by the conduction leads due to the typical spin $-1/2$ Kondo effect, thus $G(T)$ increases to its unitary limit. In such a case, the spins on the SQDs remain isolated, and hence $\mu^2(T) \approx 1/2$, and $S_{\text{HTQD}}(T) \approx 2\ln 2$. When T decreases to the scale of J_{RKKY} , spins on the SQDs are then organized parallelly [cf. $t = 0.0005$ in Fig. 12(d)]. As a result, $\mu^2(T) \approx 2/3$, and $S_{\text{HTQD}}(T) \approx \ln 3$.

For larger t , e.g., $t = 0.001$, the second screening process occurs at a low-temperature T_K^* due to a spin singlet generates between electrons on the CQD and one of the SQDs. As a result, $G(T)$ decreases to 0 gradually, associated with $\mu^2(T)$ and $S_{\text{HTQD}}(T)$ change to $1/4$ and $\ln 2$, respectively. These behaviors indicate a two-stage Kondo effect. As one may expect, with increasing t , T_K^* grows in an exponential-type function of

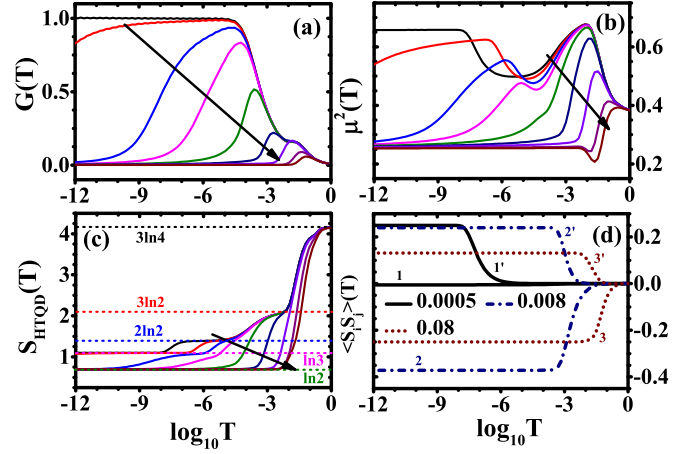


FIG. 12. Temperature-dependent (a) $G(T)$, (b) $\mu^2(T)$, (c) $S_{\text{HTQD}}(T)$, and (d) $\langle S_i S_j \rangle(T)$. Curves in panels (a)–(c) along the black arrow are for $t = 0.0005$ – 0.002 in steps of 0.0005 , 0.0035 , 0.008 , 0.02 , 0.05 , and 0.08 , respectively. Curves in (d) are for $t = 0.0005$, 0.008 , and 0.08 respectively. Those labeled by 1–3 in this panel are results for $\langle S_1 S_2 \rangle$, whereas 1'–3' are for $\langle S_2 S_3 \rangle$. The remaining parameters are the same as in Fig. 10.

T_K and J :

$$T_K^* = c_{13} T_K e^{-c_{14} T_K / J}, \quad (25)$$

which is plotted in Fig. 13, which $c_{13} = 2.61$ and $c_{14} = 0.82$. Here c_{14} is a little smaller than that in the side-coupled double dot structures, which is always of the order 1, because in our present model, the two screening temperatures are separated by J_{RKKY} .

If t becomes larger such that $t \sim \Gamma$, e.g., $t = 0.008$, then $\mu^2(T)$ and $S_{\text{HTQD}}(T)$ drop to $1/4$ and $\ln 2$ directly at a high temperature, and $\mu^2(T)$ reveals an one-peak shape. The quantum dots are then in the local moment regime with ferromagnetic Kondo coupling between the conduction band and the CQD, hence at low temperature the quantum dot spin behaves essentially as a free local moment [24,27,83,90].

When t turns to be extremely large $t \geq U_i$, e.g., $t = 0.08$, the system then moves to the MO orbital regime, with $|\langle S_i S_j \rangle|$ is reduced comparing with those in the local moment regime [cf. $t = 0.008$ and 0.08 in Fig. 12(d)].

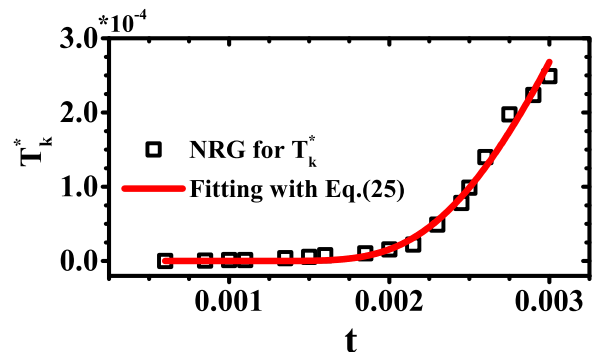


FIG. 13. T_K^* as functions of t . The remaining parameters are the same as in Fig. 10.

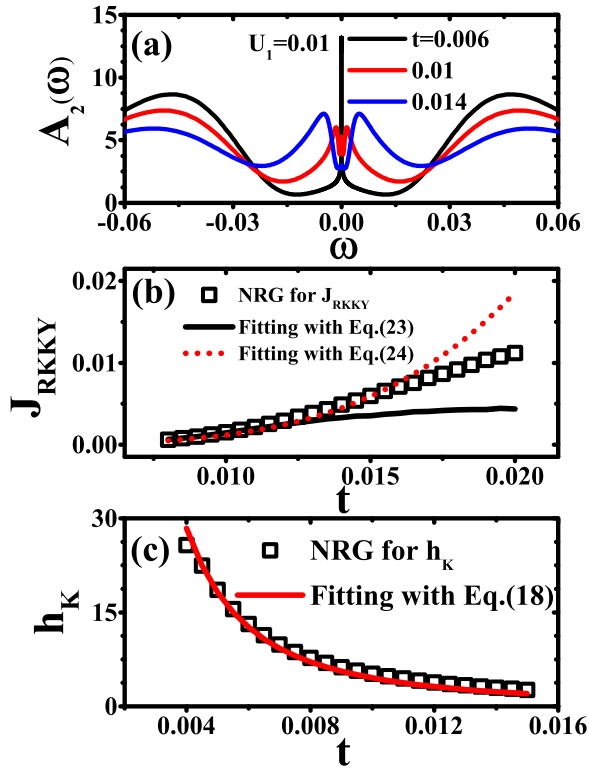


FIG. 14. (a) $A_2(\omega)$ at nearly zero temperature in terms of different t with fixed $U_1 = 0.01$. (b) The height of the Kondo peak h_K at nearly zero temperature versus of t , and its fitting function for $U_1 = 0.01$. (c) $A_2(\omega)$ at nearly zero temperature in terms of different t for the strong-interacting case with $U_1 = 0.1$. The remaining parameters are the same as Fig. 2 unless otherwise specified.

D. The RKKY interaction and side Kondo behavior for the weak-interacting CQD

We finish this section by briefly focusing on the RKKY interaction and the side Kondo behavior when the CQD is weakly interacted. In Fig. 14(a), we show $A_2(\omega)$ in terms of different t with fixed $U_1 = 0.01$. As we have expected, the RKKY peaks move away from the Fermi level when t increases. A detailed picture is given in Fig. 14(b) with squares. Furthermore, its fitting functions by Eqs. (23) and (24) are also shown in Fig. 14(b) with the fitting parameters are given by $c_{11} = 0.25$ and $c_{12} = 1.35$. Again, one finds both equations are consistent with our NRG results when t is small; however, Eq. (23) deviates very quickly from our numerical results when t is larger. Additionally, the Kondo peak is also suppressed gradually as t increases, and its height h_K could also be illustrated by Eq. (18), with $c_5 = 0.14$ [cf. Fig. 14(c)]. Because for weakly interacted CQD, the width of the peak at the Fermi level is very close to Γ .

V. QUANTUM PHASE TRANSITION AND DICKE EFFECT: EFFECT OF ϵ_1

In a similar linear structure of three quantum dots, G. Chiappe *et al.* found that the measurement of the linear conductance varying with the charge of the central dot could be an efficient readout procedure, when the system operates as

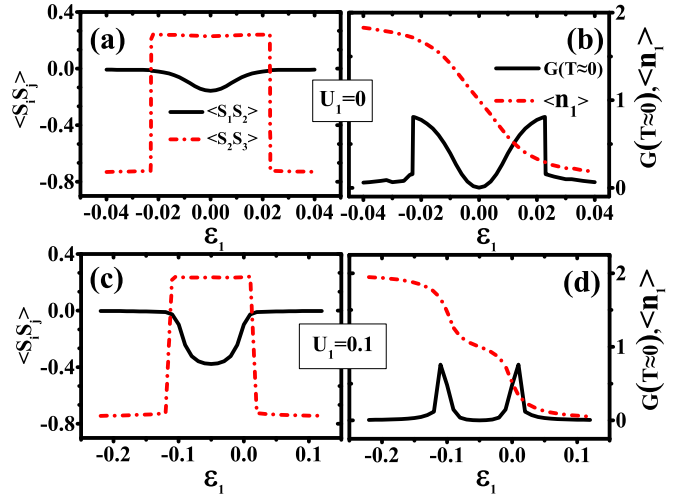


FIG. 15. [(a) and (c)] $\langle S_i S_j \rangle$ and [(b) and (d)] $G(T \approx 0)$ and charge occupation on the CQD $\langle n_1 \rangle$ versus ϵ_1 at nearly zero temperature. The results are for $U_1 = 0.0$ [(a) and (b)] and $U_1 = 0.1$ [(c) and (d)], respectively. The remaining parameters are given by $U_2 = 0.1$, $\Gamma = 0.01$, $t = 0.01$, and $\epsilon_2 = -U_2/2$.

a quantum gate with the aid of the logarithmic discretization embedded cluster approximation [91]. Here we show that similar behaviors may also emerge in our system when ϵ_1 is tuned via a gate potential. The left panels in Fig. 15 show $\langle S_i S_j \rangle$ at nearly zero temperature as a function of ϵ_1 for $U_1 = 0$ [Fig. 15(a)] and 0.1 [Fig. 15(c)], respectively, with each SQD is singly occupied. It is seen that charging the CQD triggers QPTs from an antiferromagnetic correlation between the SQDs to a ferromagnetic one, then to an antiferromagnetic one, regardless of whether the CQD is strongly or noncorrelated. These QPTs are associated with the maximum of $G(T \approx 0)$ and the processes where the charge number of the CQD $\langle n_1 \rangle$ increases from 0 (1) to 1 (2) [cf. Fig. 15(b) and Fig. 15(d)].

Above behaviors could be attributed to the following pictures. When ϵ_1 is low enough, e.g., $\epsilon_1 = -0.03$ for $U_1 = 0$, the CQD is nearly fully occupied, thus the spins on the SQDs decouple from that on the CQD with $\langle S_1 S_2 \rangle \approx 0$. Under such a situation, the ground state of the isolated quantum dots with $t = 0$ is a many-body state where spins on the SQDs are antiferromagnetically correlated. This state persists even when the CQD hybridizes with the conduction leads [91]. The spectral weight of $A_1(\omega = 0)$ is nearly zero, see Fig. 16(a), hence $G(T \approx 0) \approx 0$. However, there exists a broad peak located at about ϵ_1 , which refers to the energy of removing an electron from the CQD. On the other hand, the spectral weight of $A_2(\omega)$ is nearly symmetric with respect to $\omega = 0$, with two Coulomb peaks located at $\pm U/2$, respectively. If ϵ_1 is in the high conductance regime, then one notices two sharp peaks develop at the Fermi levels of both $A_1(\omega)$ and $A_2(\omega)$, respectively [cf. Fig. 16(b)], which then reveal line shapes of the Dicke effect [92,93]. In this case, $A_1(\omega)$ could be written as a superposition of a broad and a sharp peak, associated with long- and short-lived states, respectively. The former state, coupled to the conduction baths through Γ , is called superradiant, whereas the latter state, coupled to the SQDs

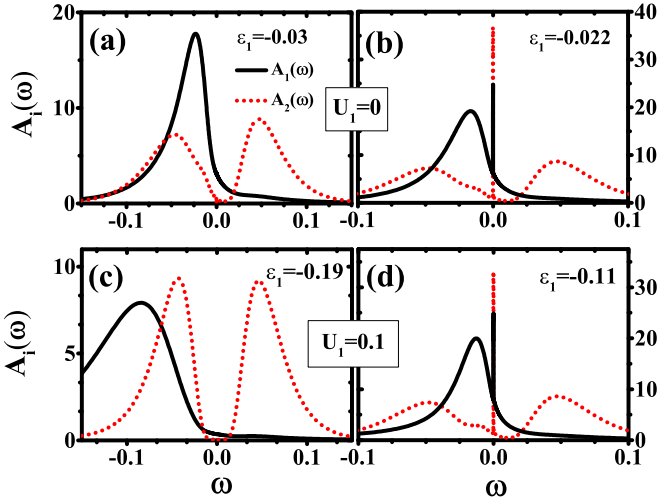


FIG. 16. [(a)–(d)] The LDOS of the quantum dots $A_i(\omega)$ ($i = 1, 2$) at nearly zero temperature in terms of different ϵ_1 , with fixed $U_1 = 0.0$ [(a) and (b)] and $U_1 = 0.1$ [(c) and (d)]. The remaining parameters are the same as in Fig. 15 unless stated otherwise.

through t , is called subradiant. When ϵ_1 moves to this regime, quantum interference in $A_1(\omega)$ through these two different couplings occurs, and a δ -like shape exhibits at the Fermi level. One expects a significant enhancement of the linear conductance. This phenomenon resembles the Dicke effect in quantum optics [94] and has been predicted in some QD structures [92,93,95–97]. As for $A_2(\omega)$, the Dicke effect is resulted from the quantum interference between the direct coupling with the CQD and the indirect coupling with the conduction bands. For strong $U_1 = 0.1$, the above discussions also apply, indicating the effect of local repulsion in the CQD can be neglected. We note that above argument is distinguished from that in Ref. [91], where the enhancement of the conductance was attributed to the Kondo effect.

VI. CROSSOVER FROM THE SIDE KONDO EFFECT TO THE FERROMAGNETIC KONDO EFFECT: EFFECT OF U_1

We finish our discussion by analyzing the effect produced by changing U_1 . From above discussions, we know that for a fixed t , when U_1 is zero, our model behaves as a PDQD model connected to conduction bath with nonconstant DOS, whereas if U_1 is large enough, then it goes into the local-moment phase. In this section, we show that by tuning U_1 , it allows to study the crossover between the side Kondo state and the local moment phase. In Figs. 17(a) and 17(b), we show $A_2(\omega)$ at nearly zero temperature for $U_1 = 0$ and 0.01, respectively, with fixed $t = 0.005$. It is seen that the Kondo peak is suppressed gradually as U_1 increases. In Fig. 17(c), we illustrate the height of the side Kondo peak h_K at nearly zero temperature versus U_1 , and its fitting function. One may see that in the large- U_1 regime satisfying $U_1 \geq 4\Gamma$, h_K could be well illustrated by the following function:

$$h_K = c_{15} \frac{T_K}{\pi t^2}, \quad (26)$$

with $c_{15} = 0.04$ and T_K is given by Eq. (21) and thus is U_1 dependent. However, if $U_1 \sim \Gamma$ or $U_1 < \Gamma$, then this func-

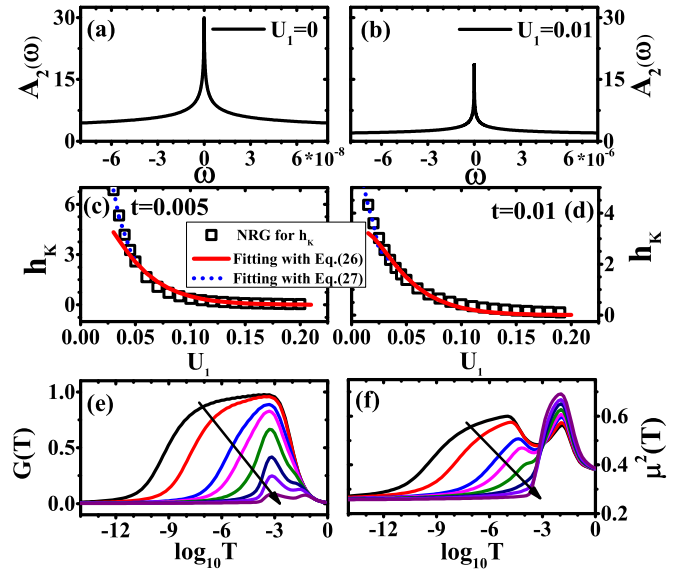


FIG. 17. [(a) and (b)] $A_2(\omega)$ at nearly zero temperature for $U_1 = 0$ and 0.01, respectively. [(c) and (d)] The height of the side Kondo peak h_K at nearly zero temperature versus U_1 for fixed $t = 0.005$ (c) and 0.01 (d) and their fitting functions. (e) $G(T)$ and (f) $\mu^2(T)$ as functions of temperature T in terms of different U_1 . Curves in panels (e) and (f) along the black arrow are for $U_1 = 0, 0.01, 0.03, 0.04, 0.06, 0.09, 0.12$, and 0.19, respectively. The remaining parameters are given by $U_2 = 0.1$, $\Gamma = 0.01$, $t = 0.005$, and $\epsilon_i = -U_i/2$ unless stated otherwise.

tion deviates from our NRG results. Because under such a circumstance, the Kondo effect in the CQD cannot generate, and hence the full width at half maximum of $A_1^0(\omega)$ is not T_K . In this case, we extract the width of $A_1^0(\omega)$, which is denoted as \tilde{W}_p , directly from our NRG results. One finds

$$h_K = c_{16} \frac{\tilde{W}_p}{\pi t^2}. \quad (27)$$

However, it is worthwhile to note that one can hardly use an identical proportionality factor in this regime. More specifically, the fitting parameter c_{16} decreases slightly as U_1 increases, e.g., with $c_{16} = 0.13$ for $U_1 = 0$ and $c_{16} = 0.03$ for $U_1 = 0.035$. These behaviors also apply to any fixed t , as is shown for example for $t = 0.01$ in Fig. 17(d) with $c_{15} = 0.09$. Furthermore, such a crossover could also be identified in $G(T)$ and $\mu^2(T)$. For small U_1/t , a plateau exists in $G(T)$ for intermediate T , accompanied by $\mu^2(T)$, revealing a two-peak shape, whereas if U_1/t is large enough, then the plateau is suppressed, and only one peak could be found in $\mu^2(T)$, due to the ferromagnetic Kondo effect.

VII. CONCLUSION

To conclude, we have studied the dynamic and thermodynamic properties of a hybrid tripartite quantum dot device, with one QD embedded in two electrodes, and the other two QDs side coupled to the central one. By modeling this system using a triple-impurity Anderson model, we first focused our attentions on the case where the CQD is noninteracting. The destructive quantum interference, the RKKY interaction,

the side Kondo effect and its suppression, and their temperature dependence are studied in detail, highlighting their relations with the band-CQD hybridization Γ , the CQD-SQD tunnelling t , the on-site electron-electron Coulomb repulsion U_i , as well the temperature T . For the purpose of comparison, results for the weak- and strong-interacting CQD are also mentioned. Furthermore, by tuning the charge of the CQD, the spin correlation between two SQDs transits from an antiferromagnetic type to a ferromagnetic one, and then to an antiferromagnetic one, regardless of whether the CQD is strongly or noncorrelated. The enhancement of the conductance is found to be associated with the Dicke effect, distinguishing from previous works. When the Coulomb repulsion in the CQD sweeps, our present structure acts as an ideal prototype revealing a crossover from an effective PDQD model to the ferromagnetic Kondo phase, and the relation of the height of the side Kondo peak is well established.

Noticing the width of the peak at the Fermi level of the central dot without t , viz., $A_1^0(\omega)$, is nearly 2Γ for the non- and weak-interacting case, while is T_K for a finite strong U_1 . By defining \tilde{W}_p as the effective bandwidth for all scales of U_1 , as has been given in Sec. VI, and combining Eqs. (17) and (24), one then obtains a unified formula of the RKKY interaction:

$$J_{\text{RKKY}} \propto \frac{t^4}{U_2 \tilde{W}_p^2}. \quad (28)$$

We stress that J_{RKKY} only associates with the quantity of $A_1^0(\omega)$ at the Fermi surface. It is noted that \tilde{W}_p is also associated with the effective scattering rate. In the perturbative formula it is Γ , whereas in the Kondo renormalized case it is T_K .

When U_1/t is small, Eqs. (18) and (27) are well suitable for describing the height of the side Kondo peak regardless of whether the CQD is non- or weakly interacted, whereas if U_1/t is strong, then Eq. (26) matches well with the numerical results. One then obtains a unified formula for the height of the side Kondo effect h_K :

$$h_K \propto \frac{\tilde{W}_p}{\pi t^2}. \quad (29)$$

In addition, for a noninteracting CQD, the local spin in the SQDs is partially screened at T_K^* , which satisfies an exponential function of Γ , whereas for a finite strong U_1 , a two-stage Kondo effect occurs for $J \ll \Gamma$. Combining Eqs. (20) and (25), one also gets a universal relation for T_K^* suitable for the non-, weak-, and strong-interacting cases:

$$T_K^* = a \tilde{W}_p e^{-b \tilde{W}_p / J}, \quad (30)$$

which is also applicable for illustrating the relation between \tilde{W}_p and the width of the Fano antiresonance dip W_F by replacing T_K^* with W_F [cf. Eqs. (13) and (22)].

ACKNOWLEDGMENTS

This work is financially supported by NSFC under Grant No. 11504102, the Hubei Key Laboratory of Automotive Power Train and Electronics [Hubei University of Automotive Technology (HUAT)] under Grant No. ZDK1202001, and the Hubei Key Laboratory of Critical Materials of New Energy Vehicles (HUAT) under Grant No. QCCLSZK2021A05.

-
- [1] P. G. Derry, A. K. Mitchell, and D. E. Logan, Quasiparticle interference from magnetic impurities, *Phys. Rev. B* **92**, 035126 (2015).
 - [2] K. Akkaravarawong, J. I. Väyrynen, J. D. Sau, E. A. Demler, L. I. Glazman, and N. Y. Yao, Probing and dressing magnetic impurities in a superconductor, *Phys. Rev. Research* **1**, 033091 (2019).
 - [3] K. Vladár and A. Zawadowski, Theory of the interaction between electrons and the two-level system in amorphous metals. I. Noncommutative model Hamiltonian and scaling of first order, *Phys. Rev. B* **28**, 1564 (1983).
 - [4] C. Xu, A. Poudel, and M. G. Vavilov, Nonadiabatic dynamics of a slowly driven dissipative two-level system, *Phys. Rev. A* **89**, 052102 (2014).
 - [5] S. M. Cronenwett, T. H. Oosterkamp, and L. P. Kouwenhoven, A tunable Kondo effect in quantum dots, *Science* **281**, 540 (1998).
 - [6] S. De Franceschi, S. Sasaki, J. M. Elzerman, W. G. van der Wiel, S. Tarucha, and L. P. Kouwenhoven, Electron Cotunneling in a Semiconductor Quantum Dot, *Phys. Rev. Lett.* **86**, 878 (2001).
 - [7] G. Katsaros, J. Kukučka, L. Vukušić, H. Watzinger, F. Gao, T. Wang, J.-J. Zhang, and K. Held, Zero field splitting of heavy-hole states in quantum dots, *Nano Lett.* **20**, 5201 (2020).
 - [8] F. Evers, R. Korytár, S. Tewari, and J. M. van Ruitenbeek, Advances and challenges in single-molecule electron transport, *Rev. Mod. Phys.* **92**, 035001 (2020).
 - [9] T. Fu, K. Frommer, C. Nuckolls, and L. Venkataraman, Single-molecule junction formation in break-junction measurements, *J. Phys. Chem. Lett.* **12**, 10802 (2021).
 - [10] T. Jamneala, V. Madhavan, and M. F. Crommie, Kondo Response of a Single Antiferromagnetic Chromium Trimer, *Phys. Rev. Lett.* **87**, 256804 (2001).
 - [11] Q. L. Li, C. Zheng, R. Wang, B. F. Miao, R. X. Cao, L. Sun, D. Wu, Y. Z. Wu, S. C. Li, B. G. Wang, and H. F. Ding, Role of the surface state in the Kondo resonance width of a Co single on Ag(111), *Phys. Rev. B* **97**, 035417 (2018).
 - [12] A. C. Hewson, *The Kondo Problem to Heavy Fermions* (Cambridge University Press, Cambridge, UK, 1997).
 - [13] S. Kumar, P. K. Ahluwalia, and K. C. Sharma, Competition between Kondo effect and RKKY interactions in heavy-fermion systems: Transport properties, *Phys. Rev. B* **56**, 3140 (1997).
 - [14] M. Amusia and V. Shaginyan, *Strongly Correlated Fermi Systems: A New State of Matter* (Springer, Cham, 2020).
 - [15] W. H. Appelt, A. Droghetti, L. Chioncel, M. M. Radonjić, E. Munöz, S. Kirchner, D. Vollhardt, and I. Rungger, Predicting the conductance of strongly correlated molecules: The Kondo effect in perchlorotriphenylmethyl/Au junctions, *Nanoscale* **10**, 17738 (2018).

- [16] P. W. Anderson, Localized magnetic states in metals, *Phys. Rev.* **124**, 41 (1961).
- [17] R. Bulla, T. A. Costi, and T. Pruschke, Numerical renormalization group method for quantum impurity systems, *Rev. Mod. Phys.* **80**, 395 (2008).
- [18] J. Kondo, Resistance minimum in dilute magnetic alloys, *Prog. Theor. Phys.* **32**, 37 (1964).
- [19] K. G. Wilson, The renormalization group: Critical phenomena and the Kondo problem, *Rev. Mod. Phys.* **47**, 773 (1975).
- [20] P. Jarillo-Herrero, J. Kong, H. S. J. van der Zant, C. Dekker, L. P. Kouwenhoven, and S. De Franceschi, Orbital Kondo effect in carbon nanotubes, *Nature (Lond.)* **434**, 484 (2005).
- [21] M. Karolak, D. Jacob, and A. I. Lichtenstein, Orbital Kondo Effect in Cobalt-Benzene Sandwich Molecules, *Phys. Rev. Lett.* **107**, 146604 (2011).
- [22] N. Roch, S. Florens, T. A. Costi, W. Wernsdorfer, and F. Balestro, Observation of the Underscreened Kondo Effect in a Molecular Transistor, *Phys. Rev. Lett.* **103**, 197202 (2009).
- [23] M. Misiorny, I. Weymann, and J. Barnaś, Underscreened Kondo effect in $S = 1$ magnetic quantum dots: Exchange, anisotropy, and temperature effects, *Phys. Rev. B* **86**, 245415 (2012).
- [24] J. A. Andrade, D. J. García, and P. S. Cornaglia, Ferromagnetic and underscreened Kondo behavior in quantum dot arrays, *Phys. Rev. B* **92**, 165416 (2015).
- [25] I. Kuzmenko, T. Kuzmenko, and Y. Avishai, Model for two-channel Kondo effect in carbon nanotube quantum dots, *Phys. Rev. B* **90**, 195129 (2014).
- [26] D. B. Karki and M. N. Kiselev, Quantum thermoelectric and heat transport in the overscreened Kondo regime: Exact conformal field theory results, *Phys. Rev. B* **102**, 241402(R) (2020).
- [27] P. P. Baruselli, R. Requist, M. Fabrizio, and E. Tosatti, Ferromagnetic Kondo Effect in a Triple Quantum Dot System, *Phys. Rev. Lett.* **111**, 047201 (2013).
- [28] P. Petit, C. Feuillet-Palma, M. L. Della Rocca, and P. Lafarge, Universality of the two-stage Kondo effect in carbon nanotube quantum dots, *Phys. Rev. B* **89**, 115432 (2014).
- [29] G.-Y. Yi, C. Jiang, L.-L. Zhang, S.-R. Zhong, H. Chu, and W.-J. Gong, Manipulability of the Kondo effect in a T-shaped triple-quantum-dot structure, *Phys. Rev. B* **102**, 085418 (2020).
- [30] X. Guo, Q.-h. Zhu, L.-y. Zhou, W. Yu, W.-g. Lu, and W.-j. Liang, Evolution and universality of two-stage Kondo effect in single manganese phthalocyanine molecule transistors, *Nat. Commun.* **12**, 1566 (2021).
- [31] O. Kashuba and C. Timm, Topological Kondo Effect in Transport Through a Superconducting Wire With Multiple Majorana End States, *Phys. Rev. Lett.* **114**, 116801 (2015).
- [32] B. Béri, Exact Nonequilibrium Transport in the Topological Kondo Effect, *Phys. Rev. Lett.* **119**, 027701 (2017).
- [33] A. K. Mitchell, D. Schuricht, M. Vojta, and L. Fritz, Kondo effect on the surface of three-dimensional topological insulators: Signatures in scanning tunneling spectroscopy, *Phys. Rev. B* **87**, 075430 (2013).
- [34] L. Isaev, G. Ortiz, and I. Vekhter, Tunable unconventional Kondo effect on topological insulator surfaces, *Phys. Rev. B* **92**, 205423 (2015).
- [35] L. G. G. V. Dias da Silva, N. Sandler, P. Simon, K. Ingersent, and S. E. Ulloa, Tunable Pseudogap Kondo Effect and Quantum Phase Transitions in Aharonov-Bohm Interferometers, *Phys. Rev. Lett.* **102**, 166806 (2009).
- [36] P. Stefański, Spin selective pseudogap Kondo effect in a double quantum dot interferometer with Rashba interaction, *J. Phys.: Condens. Matter* **25**, 085303 (2013).
- [37] A. K. Mitchell, M. Vojta, R. Bulla, and L. Fritz, Quantum phase transitions and thermodynamics of the power-law Kondo model, *Phys. Rev. B* **88**, 195119 (2013).
- [38] M. Vojta and R. Bulla, A fractional-spin phase in the power-law Kondo model, *Eur. Phys. J. B* **28**, 283 (2002).
- [39] A. K. Mitchell and L. Fritz, Kondo effect in three-dimensional Dirac and Weyl systems, *Phys. Rev. B* **92**, 121109(R) (2015).
- [40] G. T. D. Pedrosa, J. F. Silva, and E. Vernek, Kondo screening regimes in multi-Dirac and Weyl systems, *Phys. Rev. B* **103**, 045137 (2021).
- [41] M. A. Ruderman and C. Kittel, Indirect exchange coupling of nuclear magnetic moments by conduction electrons, *Phys. Rev.* **96**, 99 (1954).
- [42] D. C. Mattis, *The Theory of Magnetism* (Harper & Row, New York, 1965).
- [43] C.-H. Chung and W. Hofstetter, Kondo effect in coupled quantum dots with RKKY interaction: Effects of finite temperature and magnetic field, *Phys. Rev. B* **76**, 045329 (2007).
- [44] C.-H. Chung, G. Zarand, and P. Wölfle, Two-stage Kondo effect in side-coupled quantum dots: Renormalized perturbative scaling theory and numerical renormalization group analysis, *Phys. Rev. B* **77**, 035120 (2008).
- [45] H. Prüser, P. E. Dargel, M. Bouhassoune, R. G. Ulbrich, T. Pruschke, S. Lounis, and M. Wenderoth, Interplay between the Kondo effect and the Ruderman-Kittel-Kasuya-Yosida interaction, *Nat. Commun.* **5**, 5417 (2014).
- [46] Y. Utsumi, J. Martinek, P. Bruno, and H. Imamura, Indirect exchange interaction between two quantum dots in an Aharonov-Bohm ring, *Phys. Rev. B* **69**, 155320 (2004).
- [47] R. López, D. Sánchez, M. Lee, M.-S. Choi, P. Simon, and K. Le Hur, Probing spin and orbital Kondo effects with a mesoscopic interferometer, *Phys. Rev. B* **71**, 115312 (2005).
- [48] W.-Z. Wang, Kondo effect and continuous quantum phase transitions in double quantum dots with on-site and interdot repulsion and magnetic field, *Phys. Rev. B* **83**, 075314 (2011).
- [49] A. Spinelli, M. Gerrits, R. Toskovic, B. Bryant, M. Ternes, and A. F. Otte, Exploring the phase diagram of the two-impurity Kondo problem, *Nat. Commun.* **6**, 10046 (2015).
- [50] N. Nan, W. Li, P.-C. Wang, Y.-J. Hu, G.-L. Tan, and Y.-C. Xiong, Kondo effect and RKKY interaction assisted by magnetic anisotropy in a frustrated magnetic molecular device at zero and finite temperature, *Phys. Chem. Chem. Phys.* **23**, 5878 (2021).
- [51] R. M. Konik, Transport properties of multiple quantum dots arranged in parallel: Results from the Bethe ansatz, *New J. Phys.* **9**, 257 (2007).
- [52] D. F. Mross, and H. Johannesson, Two-impurity Kondo model with spin-orbit interactions, *Phys. Rev. B* **80**, 155302 (2009).
- [53] J. Hermenau, S. Brinker, M. Marciani, M. Steinbrecher, M. dos Santos Dias, R. Wiesendanger, S. Lounis, and J. Wiebe, Stabilizing spin systems via symmetrically tailored RKKY interactions, *Nat. Commun.* **10**, 2565 (2019).
- [54] S.-H. Zhang, J.-J. Zhu, W. Yang, and K. Chang, Selective generation and amplification of RKKY interactions by a $p - n$ interface, *Phys. Rev. B* **99**, 195456 (2019).
- [55] S. S. P. Parkin, N. More, and K. P. Roche, Oscillations in Exchange Coupling and Magnetoresistance in Metallic

- Superlattice Structures: Co/Ru, Co/Cr, and Fe/Cr, *Phys. Rev. Lett.* **64**, 2304 (1990).
- [56] S. S. P. Parkin and D. Mauri, Spin engineering: Direct determination of the Ruderman-Kittel-Kasuya-Yosida far-field range function in ruthenium, *Phys. Rev. B* **44**, 7131 (1991).
- [57] R. Žitko and J. Bonča, Multiple-impurity Anderson model for quantum dots coupled in parallel, *Phys. Rev. B* **74**, 045312 (2006).
- [58] A. K. Mitchell, E. Sela, and D. E. Logan, Two-channel Kondo Physics in Two-Impurity Kondo Models, *Phys. Rev. Lett.* **108**, 086405 (2012).
- [59] C. F. Hirjibehedin, C.-Y. Lin, A. F. Otte, M. Ternes, C. P. Lutz, B. A. Jones, and A. J. Heinrich, Large magnetic anisotropy of a single spin embedded in a surface molecular network, *Science* **317**, 1199 (2007).
- [60] T. Uchihashi, Jianwei Zhang, J. Kröger, and R. Berndt, Quantum modulation of the Kondo resonance of Co adatoms on Cu/Co/Cu(100): Low-temperature scanning tunneling spectroscopy study, *Phys. Rev. B* **78**, 033402 (2008).
- [61] Y. H. Jiang, W. D. Xiao, L. W. Liu, L. Z. Zhang, J. C. Lian, K. Yang, S. X. Du, and H.-J. Gao, Self-assembly of metal phthalocyanines on Pb(111) and Au(111) surfaces at submonolayer coverage, *J. Phys. Chem. C* **115**, 21750 (2011).
- [62] S. H. Choi, B. Kim, and D. C. Frisbie, Electrical resistance of long conjugated molecular wires, *Science* **320**, 1482 (2008).
- [63] H. Kim and D. Segal, Controlling charge transport mechanisms in molecular junctions: Distilling thermally induced hopping from coherent-resonant conduction, *J. Chem. Phys.* **146**, 164702 (2017).
- [64] M. Kotzian, F. Gallego-Marcos, G. Platero, and R. J. Haug, Channel blockade in a two-path triple-quantum-dot system, *Phys. Rev. B* **94**, 035442 (2016).
- [65] H.-O. Li, G. Cao, G.-D. Yu, M. Xiao, G.-C. Guo, H.-W. Jiang, and G.-P. Guo, Controlled Quantum Operations of A Semiconductor Three-Qubit System, *Phys. Rev. Appl.* **9**, 024015 (2018).
- [66] M. Urdampilleta, S. Klyatskaya, J.-P. Cleuziou, M. Ruben, and W. Wernsdorfer, Supramolecular spin valves, *Nat. Mater.* **10**, 502 (2011).
- [67] S. Gao (ed.), *Molecular Nanomagnets and Related Phenomena* (Springer Verlag, Berlin, 2014).
- [68] G. A. Timco, S. Carretta, F. Troiani, F. Tuna, R. J. Pritchard, C. A. Muryn, E. J. L. McInnes, A. Ghirri, A. Candini, P. Santini, G. Amoretti, M. Affronte, and R. E. P. Winpenny, Engineering the coupling between molecular spin qubits by coordination chemistry, *Nat. Nanotechnol.* **4**, 173 (2009).
- [69] H. Cui, Z.-B. Hu, C. Chen, H. Ruan, Y. Fang, L. Zhang, Y. Zhao, G. Tan, Y. Song, and X. Wang, A high-spin diradical dianion and its bridged chemically switchable single-molecule magnet, *Chem. Sci.* **12**, 9998 (2021).
- [70] A. Calzolari, A. Rajca, and M. B. Casu, From radical to triradical thin film processes: The Blatter radical derivatives, *J. Mater. Chem. C* **9**, 10787 (2021).
- [71] E. Macaluso, M. Rubín, D. Aguilà, A. Chiesa, L. A. Barrios, J. I. Martínez, P. J. Alonso, O. Roubeau, F. Luis, G. Aromí, and S. Carretta, A heterometallic [LnLn'Ln] lanthanide complex as a qubit with embedded quantum error correction, *Chem. Sci.* **11**, 10337 (2020).
- [72] H. R. Krishna-murthy, J. W. Wilkins, and K. G. Wilson, Renormalization-group approach to the Anderson model of dilute magnetic alloys. I. Static properties for the symmetric case, *Phys. Rev. B* **21**, 1003 (1980).
- [73] R. Žitko and T. Pruschke, Energy resolution and discretization artifacts in the numerical renormalization group, *Phys. Rev. B* **79**, 085106 (2009).
- [74] R. Landauer, Spatial variation of currents and fields due to localized scatterers in metallic conduction, *IBM J. Res. Dev.* **1**, 223 (1957).
- [75] Y. Meir, N. S. Wingreen, and P. A. Lee, Low-Temperature Transport Through a Quantum Dot: The Anderson Model Out of Equilibrium, *Phys. Rev. Lett.* **70**, 2601 (1993).
- [76] A. Weichselbaum and J. von Delft, Sum-rule Conserving Spectral Functions From the Numerical Renormalization Group, *Phys. Rev. Lett.* **99**, 076402 (2007).
- [77] F. B. Anders and A. Schiller, Real-Time Dynamics in Quantum-Impurity Systems: A Time-Dependent Numerical Renormalization-Group approach, *Phys. Rev. Lett.* **95**, 196801 (2005).
- [78] T. V. Shabbazyan and M. E. Raikh, Two-channel resonant tunneling, *Phys. Rev. B* **49**, 17123 (1994).
- [79] P. S. Cornaglia and D. R. Grempel, Strongly correlated regimes in a double quantum dot device, *Phys. Rev. B* **71**, 075305 (2005).
- [80] R. Žitko, Fano-Kondo effect in side-coupled double quantum dots at finite temperatures and the importance of two-stage Kondo screening, *Phys. Rev. B* **81**, 115316 (2010).
- [81] J. A. Andrade, P. S. Cornaglia, and A. A. Aligia, Transport through side-coupled multilevel double quantum dots in the Kondo regime, *Phys. Rev. B* **89**, 115110 (2014).
- [82] P. C. Wang, Y. H. Wang, C. Chen, J. Zhang, W. Li, N. Nan, J. N. Wang, J. T. Yang, A. Laref, and Y. C. Xiong, Frustration-controlled quantum phase transition between multiple singular two-stage Kondo behaviors in a tetrahedral quadruple quantum dot structure, *Phys. Rev. B* **105**, 075430 (2022).
- [83] A. K. Mitchell, T. F. Jarrold, M. R. Galpin, and D. E. Logan, Local moment formation and Kondo screening in impurity trimers, *J. Phys. Chem. B* **117**, 12777 (2013).
- [84] L. G. G. V. Dias da Silva, N. P. Sandler, K. Ingersent, and S. E. Ulloa, Zero-Field Kondo Splitting and Quantum-Critical Transition in Double Quantum Dots, *Phys. Rev. Lett.* **97**, 096603 (2006).
- [85] D. C. Langreth, Friedel sum rule for Anderson's model of localized impurity states, *Phys. Rev.* **150**, 516 (1966).
- [86] T. K. Ng and P. A. Lee, On-Site Coulomb Repulsion and Resonant Tunneling, *Phys. Rev. Lett.* **61**, 1768 (1988).
- [87] F. D. M. Haldane, Theory of the atomic limit of the Anderson model. I. Perturbation expansions re-examined, *J. Phys. C* **11**, 5015 (1978).
- [88] T. A. Costi, A. C. Hewson, and V. Zlatić, Transport coefficients of the Anderson model via the numerical renormalization group, *J. Phys.: Condens. Matter* **6**, 2519 (1994).
- [89] W. Hofstetter and S. Kehrein, Symmetric Anderson impurity model with a narrow band, *Phys. Rev. B* **59**, R12732 (1999).
- [90] A. K. Mitchell, T. F. Jarrold, and D. E. Logan, Quantum phase transition in quantum dot trimers, *Phys. Rev. B* **79**, 085124 (2009).
- [91] G. Chiappe, E. V. Anda, L. C. Ribeiro, and E. Louis, Kondo regimes in a three-dots quantum gate, *Phys. Rev. B* **81**, 041310(R) (2010).

- [92] P. A. Orellana, M. L. L. de Guevara, and F. Claro, Controlling Fano and Dicke effects via a magnetic flux in a two-site Anderson model, *Phys. Rev. B* **70**, 233315 (2004).
- [93] P. A. Orellana, G. A. Lara, and E. V. Anda, Kondo and Dicke effect in quantum dots side coupled to a quantum wire, *Phys. Rev. B* **74**, 193315 (2006).
- [94] T. Brandes, Coherent and collective quantum optical effects in mesoscopic systems, *Phys. Rep.* **408**, 315 (2005).
- [95] E. Vernek, P. A. Orellana, and S. E. Ulloa, Suppression of Kondo screening by the Dicke effect in multiple quantum dots, *Phys. Rev. B* **82**, 165304 (2010).
- [96] Q. Wang, H. Xie, Y.-H. Nie, and W. Ren, Enhancement of thermoelectric efficiency in triple quantum dots by the Dicke effect, *Phys. Rev. B* **87**, 075102 (2013).
- [97] S. Głodzik, K. P. Wójcik, I. Weymann, and T. Domanski, Interplay between electron pairing and Dicke effect in triple quantum dot structures, *Phys. Rev. B* **95**, 125419 (2017).